Twin indicators of coastal vulnerability: land subsidence and mangrove extent change in Dili, Timor-Leste

Author name: Lik Ren, Tai
Affiliation: Woosong University, Daejeon, Korea
Email address: likrentai@gmail.com
University email address: likrentai@wsu.ac.kr
ORCID: https://orcid.org/0009-0002-6667-3331

Twin indicators of coastal vulnerability: land subsidence and mangrove extent change in Dili, Timor-Leste

Lik Ren Tai*

Woosong University, Daejeon, Korea (ORCID iD: 0009-0002-6667-3331)

Abstract

Mangrove forests and land subsidence are major drivers of coastal vulnerability rarely quantified together outside the well-studied deltas of Southeast Asia. This study provides the first satellite-based, twin-indicator assessment of coastal vulnerability for Dili, Timor-Leste, combining Sentinel-1 InSAR time series analysis of land subsidence with Global Mangrove Watch extent change over a multi-decadal baseline. Subsidence was detected across the urban coastal footprint (mean -0.53 cm/yr, locally exceeding -4 cm/yr) and was strongly spatially clustered, but its attribution to groundwater extraction did not survive proper spatial statistical control. Mangrove extent increased significantly over both a full 1996-2020 record and a 2007-2020 subset, contrary to national reports of long-term decline, although gross turnover exceeded net change at every transition and the most recent period showed a net loss. Mangrove-present zones fell within subsidence clusters at roughly twice the area-wide rate and none fell within stable or uplifting clusters, a categorical association not matched by a continuous relationship between the two indicators. No evidence emerged for a direct subsidence contribution to mangrove loss over the short InSAR-mangrove overlap window. Combined with regional sea-level-rise projections, the observed subsidence trend implies most of the study area could face over 0.5 m of compound relative sea-level rise by 2100 under either emissions scenario. These findings provide the first satellite geodetic measurement of subsidence in Timor-Leste and show that Dili's remaining mangroves and its subsiding zones share the same low-lying terrain, a convergence relevant to coastal planning regardless of the causal mechanisms linking them.

Keywords: InSAR, Land subsidence, Mangrove dynamics, Coastal vulnerability, Sentinel-1, Timor-Leste

Article highlights:

- First satellite InSAR subsidence measurement made anywhere in Timor-Leste.
- Groundwater-extraction attribution to subsidence did not survive spatial control.
- Mangrove extent increased significantly 1996-2020, contrary to predicted decline.
- Mangrove zones fell in subsidence clusters at twice the area-wide rate.
- By 2100, most zones may face over 0.5 m of compound relative sea-level rise.

1. Introduction

Mangrove forests and land subsidence are among the most consequential drivers of coastal vulnerability in Southeast Asia, yet they are typically studied in isolation. Mangroves attenuate wave energy, trap sediment, and buffer shorelines against inundation, providing flood protection benefits valued at tens of billions of dollars annually worldwide (Menéndez et al., 2020), while subsidence, driven predominantly by groundwater extraction from unconsolidated coastal aquifers, raises relative sea level independently of climatic sea level change and now threatens a substantial share of the global coastal population (Herrera-García et al., 2021). Where the two processes co-occur, a city can lose its principal natural coastal defence at the same time as its exposure to flooding increases, a combination that neither process captures when assessed on its own. Despite this, satellite-based studies that quantify both processes for a single city remain rare outside the well-studied deltas of Java and the Mekong.

Timor-Leste, a small, mountainous nation on the northern margin of the Banda Arc (Figure 1), illustrates this gap. Dili, the national capital, sits on a narrow coastal plain of young alluvial fan sediments, and the shallow aquifer beneath the city supplies most of its drinking water (Sarmento & Da Cruz Cardoso, 2014). Groundwater extraction from this aquifer is widely understood in the hydrogeological literature to drive surface subsidence, yet no satellite-based geodetic measurement of land subsidence has previously been made for Dili, or for any location in Timor-Leste. This is a substantial gap relative to comparable Southeast Asian coastal cities, where Interferometric Synthetic Aperture Radar (InSAR) has become the standard tool for subsidence monitoring and has revealed some of the fastest coastal subsidence rates recorded anywhere in the world (Wu et al., 2022; Minderhoud et al., 2025).

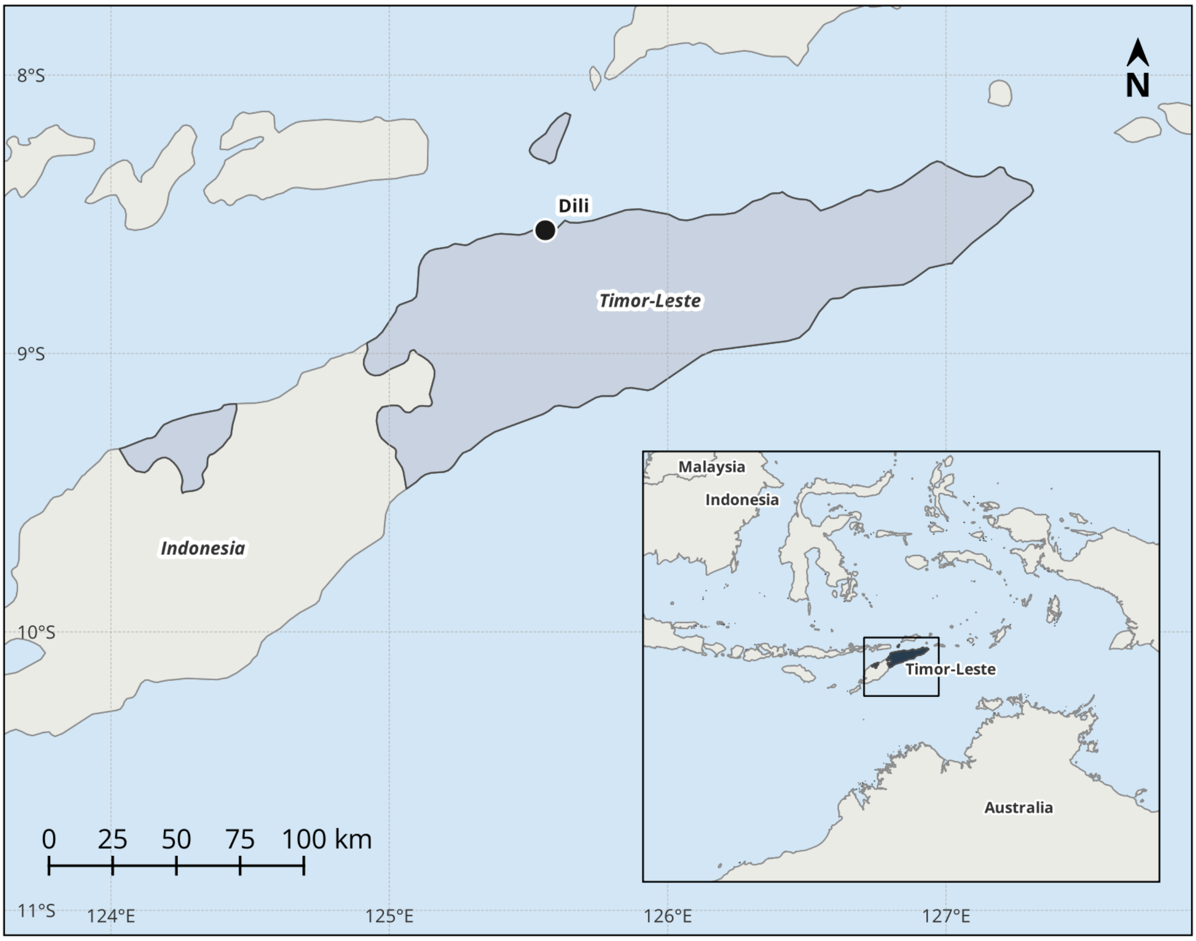

Figure 1. *Regional context of Timor-Leste. The main panel shows Timor island, with Timor-Leste and the Indonesian portion distinguished, and the location of Dili on the north coast. The inset shows the wider Southeast Asian and northern Australian setting, with the extent of the main panel indicated. Base data: Natural Earth 1:10m.*

A parallel gap exists on the mangrove side. National-level reporting has documented substantial mangrove loss across Timor-Leste since 1940, driven principally by timber and fuelwood harvesting, conversion to brackish aquaculture, and salt extraction, mirroring the aquaculture and land-use conversion pressures documented across Southeast Asia more broadly (Alongi, 2014; Richards & Friess, 2016). No study, however, has applied a consistent, multi-epoch satellite change-detection framework to Dili's coastline specifically, despite Dili concentrating much of the country's urban development pressure on a coastline where remaining mangrove stands are already fragmented and confined to a narrow band between Tibar and the Bay of Dili.

Considered together, these two processes describe a coherent risk pathway rather than two unrelated gaps in the literature. A city simultaneously losing its natural coastal buffer and becoming more exposed to flooding through subsidence faces a materially different risk profile than either process would suggest in isolation. Whether subsidence itself contributes directly to mangrove loss is a separate and more difficult question. Relative sea level rise driven by subsidence has been shown to outpace mangrove sediment accretion in Demak and Semarang, Indonesia (van Bijsterveldt et al., 2023), and a comparable dieback mechanism, sea level rise outpacing accretion during an extreme climate anomaly, has recently been documented in the Maldives (Carruthers et al., 2024). Neither mechanism has been tested in a Timor-Leste context. Because direct land-use pressure is understood to be the dominant driver of mangrove loss in Timor-Leste, this study treats a subsidence contribution as an exploratory hypothesis, and, if present, as an additional stressor rather than the primary cause.

Timor-Leste's tectonic setting strengthens the case for attributing any detected subsidence to a local, human driven process. The island sits within an actively uplifting collision zone, where the locked subduction of the Australian Plate beneath the Banda Arc has driven regional uplift over the last several million years (Harris, 2011). Subsidence measured within Dili's urban footprint would therefore represent a localised departure from this broader uplift trend, providing a stronger basis for attributing an observed subsidence signal to groundwater extraction than would be available in a setting without a clear regional tectonic baseline to depart from.

This study provides the first satellite-based, twin-indicator assessment of coastal vulnerability for Dili, pairing Sentinel-1 InSAR time series analysis of land subsidence with mangrove extent change derived from the Global Mangrove Watch (Bunting et al., 2022) over a multi-decadal baseline. Specifically, it characterises the rate and spatial pattern of land subsidence across Dili's urban coastal footprint, quantifies the rate of mangrove extent change along Dili's coastline since 1996, tests whether subsidence and mangrove loss exhibit spatially coincident patterns of vulnerability and characterises the combined risk profile the two indicators present together, and evaluates, as an exploratory analysis, whether subsidence-driven relative submergence contributes to mangrove stress beyond what direct land-use pressure alone would explain. Together, these analyses provide the first satellite geodetic measurement of land subsidence anywhere in Timor-Leste.

2. Study Area and Data

2.1 Study Area

Dili, the capital and largest city of Timor-Leste, lies on the island's northern coast facing the Ombai Strait, built on late Holocene and actively forming alluvial fan sediments within a narrow coastal plain flanked by steep, mountainous terrain to the south. The study area comprises Dili's mainland coastline between Tibar in the west and Metinaro in the east, a distance of approximately 32 km, buffered 5 km to provide spatial context beyond the immediate urban footprint (Figure 2). Elevation across this buffered area ranges from -0.76 m to 1,428.30 m, derived from the Copernicus DEM GLO-30 (Section 3.2), reflecting the abrupt transition from coastal plain to hillslope. Atauro Island, administratively part of Dili Municipality until its formal separation in 2022, lies outside this mainland focused study area and is not represented in the administrative boundary dataset used here (GADM, 2026), a data vintage mismatch with no material effect on the present analysis given the mainland only scope.

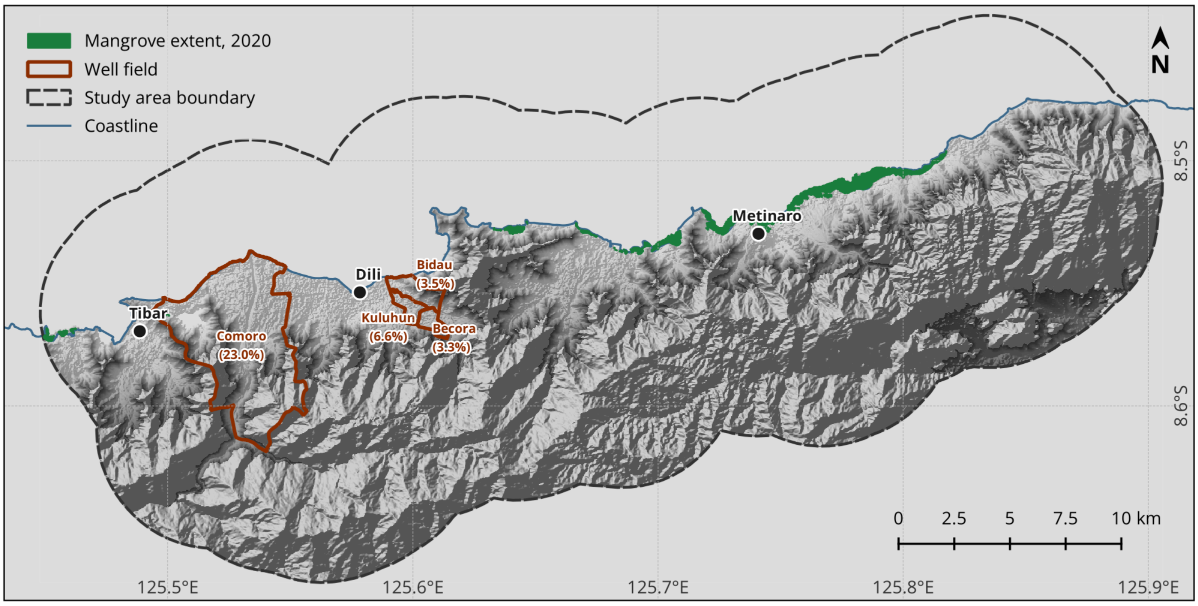

Figure 2. *Study area, Dili, Timor-Leste. The dashed line marks the study area boundary, comprising the mainland coastline between Tibar and Metinaro with a 5 km buffer. Mangrove extent is shown for 2020 (Global Mangrove Watch v3.0). Named well fields are labelled with each field's share of total municipal water supply (Sarmento & Da Cruz Cardoso, 2014). The Bedori well field is not shown; the source provides no locational information beyond the place name. Background shading is hillshaded relief derived from the Copernicus DEM GLO-30, shown for topographic context. Coordinates are WGS 84; analysis was performed in UTM Zone 51S (EPSG:32751).*

Timor-Leste's climate is governed by the West Pacific monsoon, producing a pronounced wet season between approximately December and April and a markedly drier remainder of the year, with substantial inter-annual variability linked to the El Niño-Southern Oscillation (da Costa Belo et al., 2026). This seasonality is directly relevant to the tropospheric correction applied during InSAR processing (Section 3.2) and to rainfall driven aquifer recharge, a contextual factor for the study's central groundwater subsidence mechanism.

Timor-Leste's population was projected, as of the early 2010s, to nearly triple by 2050, with growth increasingly concentrated in urban centres (Molyneux et al., 2012). As the country's primary economic and administrative centre, Dili absorbs a disproportionate share of this settlement pressure, a dynamic reflected in the built-up density predictor used in the attribution regression (Section 3.5) and the land-use conversion pressure covariate used in the exploratory RQ4 analysis (Section 3.6).

The shallow, unconfined aquifer beneath Dili is the city's primary drinking water source. Approximately 37% of total municipal water supply is drawn from a small number of named borehole fields, concentrated in Comoro to the west and in Kuluhun, Bidau, and Becora to the east, with a fifth, smaller field at Bedori (Sarmento & Da Cruz Cardoso, 2014). These named well-field locations directly inform the groundwater extraction intensity predictor used in Section 3.5.

Mangrove cover along Dili's coastline persists as a discontinuous band between Tibar and the Bay of Dili, the shrinking remnant of substantially more extensive national coverage prior to 1940 (Alongi, 2014). This remaining extent, captured across eleven epochs between 1996 and 2020 by the Global Mangrove Watch (Bunting et al., 2022), forms the basis for the mangrove change detection analysis (Section 3.3). A known limitation of C band InSAR coherence over dense vegetation canopy (Section 3.2) means the subsidence signal is comparatively less reliable directly beneath mangrove stands than over the adjacent urban footprint, a caveat relevant to interpreting the RQ3 spatial coincidence analysis (Section 3.6).

2.2 Data

Table 1 summarises the primary datasets used in this study. Full acquisition parameters and processing procedures for each dataset are described in the corresponding Methodology subsections referenced in the table.

Table 1. *Summary of datasets used in this study.*

Dataset	Source	Resolution	Coverage	Primary role
Sentinel-1 SLC	Copernicus Data Space Ecosystem	~5 × 20 m (burst)	2017–2026	InSAR subsidence (RQ1; Section 3.2)
Global Mangrove Watch v3.0	Bunting et al. (2022)	~25 m (vector)	1996–2020, 11 epochs	Mangrove extent and change (RQ2; Section 3.3)
Copernicus DEM GLO-30	European Space Agency (2022)	30 m	Static	Topographic phase removal; elevation predictor (Section 3.2, 3.5)
GHS-BUILT-S	Pesaresi et al. (2024)	100 m	2000–2020, 5 epochs	Built-up density predictor (Section 3.5, 3.6)
Well-field borehole share data	Sarmento & Da Cruz Cardoso (2014)	Field level	2014 survey	Groundwater extraction intensity predictor (Section 3.5)
Roads and coastline	OpenStreetMap contributors (2026)	Vector	Current	Distance to road, distance to coast predictors (Section 3.5)
Administrative boundaries	GADM (2026), version 4.1	Vector	Version pinned	Spatial masking; well-field geocoding (Section 3.5)
Sea level rise projections	Garner et al. (2021)	Regional grid	Scenario based, to 2100	SLR compounding (Section 3.7)

All spatial datasets were harmonised to a common coordinate reference system (WGS 84 / UTM Zone 51S, EPSG:32751) prior to analysis.

3. Methodology

3.1 Analytical Framework and Zonal Unit of Analysis

Land subsidence and mangrove extent change were characterised independently before being jointly analysed. Subsidence was derived from Sentinel-1 InSAR time series analysis (Section 3.2) and mangrove extent change from Global Mangrove Watch products (Section 3.3), addressing RQ1 and RQ2 respectively. The two indicators were then tested for spatial coincidence and combined risk profile (RQ3, Section 3.6) and, as an exploratory analysis, for a subsidence driven contribution to mangrove stress beyond direct land-use pressure (RQ4, Section 3.6).

All zonal statistics were computed on a regular grid rather than at the pixel level, to balance spatial resolution against the small sample risk inherent to a single, compact study site. Three candidate grid sizes (100 m, 250 m, 500 m) were evaluated against usable zone count, the stability of Global Moran's I on zonal subsidence rate, and the stability of attribution regression coefficient signs and significance (Table S1). A 250 m grid, yielding 12,781 usable zones (defined as cells with valid pixel coverage at or above 50% of the theoretical per cell maximum), was selected as the final spatial unit for all subsequent zonal analyses (Sections 3.4 to 3.6) and is used throughout the Results.

3.2 InSAR Time Series Processing

Sentinel-1 Single Look Complex acquisitions on a single ascending relative orbit, spanning 2017 to 2026, were processed via the Alaska Satellite Facility's HyP3 on demand cloud service, using its burst based interferometric processing pipeline built on ISCE2, the InSAR Scientific Computing Environment (HyP3 product type: INSAR_ISCE_MULTI_BURST). A five burst subset covering the Tibar to Metinaro coastline was identified by direct intersection of the study area with ASF's burst catalogue. Candidate interferometric pairs were constructed using a temporal neighbour Small Baseline Subset (SBAS) scheme (Berardino et al., 2002), connecting each acquisition to its three nearest chronological neighbours, and were subsequently filtered on perpendicular baseline (threshold 150 m) to limit geometric decorrelation. The resulting network comprised 737 interferograms spanning 273 unique acquisition dates. Velocities are reported in the Sentinel-1 line-of-sight geometry rather than converted to vertical displacement. This follows common practice for InSAR-based subsidence studies under an assumption of predominantly vertical deformation; a single-geometry ascending-only acquisition cannot independently resolve a horizontal component, so a spatially localised horizontal contribution to the reported rates cannot be fully excluded.

Time series inversion followed the SBAS approach as implemented in MintPy (Yunjun et al., 2019). The reference pixel was selected by intersecting average temporal coherence, elevation, and mask validity criteria across the study area, together with a minimum distance constraint from the named well-field locations, to avoid referencing the displacement time series to a point that might itself be subject to extraction driven motion. The selected reference point, near Metinaro at the eastern edge of the study area, sits 21 to 37 km from the Tibar to Metinaro coastal strip and the named well fields, a consequence of the mask validity constraint; this distance is a limitation to bear in mind when interpreting absolute displacement magnitudes near either extremity of the study area. The linear phase ramp removal described below is the primary mitigation for the long-wavelength bias this reference-point distance could otherwise introduce across the 32 km study area.

Phase unwrapping errors, found to be widespread across the coastal study area, were corrected using a phase closure approach. Tropospheric delay was estimated from ERA5 reanalysis fields (Hersbach et al., 2020) and removed prior to inversion. A linear phase ramp was subsequently removed, appropriate for a spatially localised deformation signal rather than a long wavelength tectonic or atmospheric artefact, and topographic residual phase was corrected following Fattahi and Amelung (2013). Acquisition dates were screened for excessive residual root mean square error relative to the network median prior to final velocity estimation. Elevation, used both for topographic phase removal here and as an attribution regression predictor (Section 3.5), was sourced from the Copernicus DEM GLO-30 (European Space Agency, 2022).

3.3 Mangrove Extent and Change Detection

Mangrove extent was derived directly from Global Mangrove Watch version 3.0 (Bunting et al., 2022), which provides vector mangrove extent products for eleven discrete epochs between 1996 and 2020 (1996, 2007 to 2010, 2015 to 2020) derived from a combination of L band synthetic aperture radar and optical satellite data. No independent classification was performed. All eleven epochs were clipped to a coastal study area buffered 5 km around the Dili mainland coastline, and per epoch extent was computed by summation of clipped polygon area after reprojection to a local UTM zone.

Two temporal groupings were used for different purposes: the full eleven epoch series (1996 to 2020) for the long term trend analysis (Section 3.4), and the three epoch subset overlapping the InSAR observation period (2018 to 2020) for the comparative and exploratory analyses (Section 3.6). Mangrove loss and gain were computed geometrically, via polygon intersection and difference, for each consecutive epoch pair in the long term series and for the direct 2018 to 2020 span used in the InSAR overlap analyses.

3.4 Trend Analysis

Trend direction and significance for both the zonal subsidence time series and the mangrove extent series were assessed using the Mann-Kendall test (Mann, 1945), a rank based non parametric test that does not assume a particular data distribution. Given the potential for serial autocorrelation in both series, the Hamed-Rao modification (Hamed & Rao, 1998), which adjusts the test variance for autocorrelated observations, was applied alongside the standard test. Trend magnitude was estimated using the Theil-Sen slope estimator (Sen, 1968), computed on a real calendar time axis rather than an observation index axis in both cases, since neither the Sentinel-1 revisit record nor the multi decadal mangrove epoch series is evenly spaced in time; an index based slope would misstate the true annualised rate under non uniform spacing.

For the subsidence series, trend testing was applied to the full per zone displacement time series (273 dates) rather than to the already collapsed mean velocity, since the Hamed-Rao correction requires the underlying observations. For the mangrove series, trend testing was applied separately to the full 1996 to 2020 series and to a 2007 to 2020 robustness subset excluding the earliest epoch, given a known methodological step change between the sparser Landsat era 1996 GMW input and the denser multi sensor compositing used from 2007 onward.

3.5 Spatial Autocorrelation and Attribution Regression

Spatial autocorrelation in zonal subsidence rate was assessed using Global Moran's I (Moran, 1950) under queen contiguity weights. Local spatial clustering was mapped using Local Indicators of Spatial Association (Anselin, 1995), classifying each zone as a member of a high-high (stable or uplifting) cluster, a low-low (subsiding) cluster, a spatial outlier, or not significant, at a permutation based significance threshold.

Subsidence rate was regressed against five standardised predictors: elevation (Copernicus DEM GLO-30; European Space Agency, 2022), built-up density (Global Human Settlement Layer GHS-BUILT-S, five epochs 2000 to 2020; Pesaresi et al., 2024), well-field extraction intensity (a zonal fill surface built from named well-field borehole share data reported in Sarmento and Da Cruz Cardoso, 2014, geocoded to administrative boundaries from the Database of Global Administrative Areas (GADM, 2026)), distance to road, and distance to coast (both derived from OpenStreetMap; OpenStreetMap contributors, 2026). Built-up density values were sampled with the source raster's no data value passed explicitly to the zonal statistics function, to prevent sentinel values at water body edges from being silently averaged into valid predictor means.

An ordinary least squares specification was fitted first, followed by Lagrange Multiplier diagnostics (Anselin et al., 1996) on the OLS residuals to test for spatial dependence and to discriminate between a Spatial Lag and a Spatial Error specification. Where the diagnostics favoured a Spatial Error Model, this was estimated via the generalised moments estimator of Kelejian and Prucha (1999), with a heteroskedasticity robust variant (Kelejian & Prucha, 2010) fitted as a robustness check against the assumption of homoskedastic disturbances.

3.6 Comparative Synthesis and Exploratory Attribution

For RQ3, subsidence and mangrove loss were compared over the 2018 to 2020 InSAR overlap window, the only period in which the two records genuinely overlap in time. Zones containing 2018 mangrove extent were identified on the 250 m grid and cross tabulated against their LISA cluster classification (Section 3.5) to test for categorical spatial coincidence between mangrove presence and subsidence clustering. A continuous per zone mangrove loss rate (loss area divided by 2018 baseline area) was correlated against zonal subsidence rate using Spearman's rank correlation. Because a small-baseline area can produce a spuriously extreme percentage loss rate from a small absolute change, this correlation was computed both for the full zone set and for a subset restricted to zones with a 2018 baseline area of at least 0.5 ha, as a robustness check against small denominator noise.

For RQ4, zones were split into high and low subsidence groups using two independent schemes: a median split on zonal subsidence rate as the primary specification, and a tertile split (top and bottom thirds, middle third excluded) as a robustness check, since the LISA cluster classification used elsewhere could not be reused here. Land-use conversion pressure, the primary alternative explanation for mangrove loss, was operationalised as the change in built-up density between 2015 and 2020, bracketing the mangrove loss observation window, distinct from the static built-up density level used as a predictor in Section 3.5. Group differences in mangrove loss rate were tested using the Mann-Whitney U test (unadjusted) and an ordinary least squares specification with conversion pressure included as a covariate (adjusted), for both the median split and tertile split groupings.

3.7 Sea Level Rise Compounding

To place the observed subsidence rate in the context of future relative sea level exposure, each zone's Theil-Sen subsidence slope (Section 3.4) was linearly extrapolated forward from the end of the InSAR observation record to two future horizons, 2050 and 2100, and combined additively with regional sea level rise projections from the NASA/IPCC AR6 Sea Level Projection Tool (Garner et al., 2021) for two emissions scenarios, SSP2-4.5 and SSP5-8.5 (IPCC Shared Socioeconomic Pathways corresponding to moderate and high greenhouse gas emissions trajectories, respectively). This combination is presented as a bounded trend extrapolation rather than a scenario based predictive model: it holds the observed geodetic rate constant over the extrapolation window and does not attempt to model future changes in extraction intensity, urbanisation, or the physical drivers of subsidence itself.

4. Results

4.1 RQ1: Land Subsidence Rate and Spatial Pattern

Across the 250 m zonal grid (n = 12,781), mean subsidence over the observation period was -0.530 cm/yr (SD = 0.655), ranging from -4.260 to +2.606 cm/yr (Figure 3). Hamed-Rao Modified Mann-Kendall trend testing on the full per-zone displacement time series found a significant decreasing trend (ongoing subsidence) in 9,246 zones (72.4%) and a significant increasing trend (uplift) in 1,162 zones (9.1%); 2,371 zones (18.5%) showed no significant trend, and 2 zones (0.02%) returned an undefined result due to a known edge case in the Hamed-Rao variance correction formula at very low residual autocorrelation.

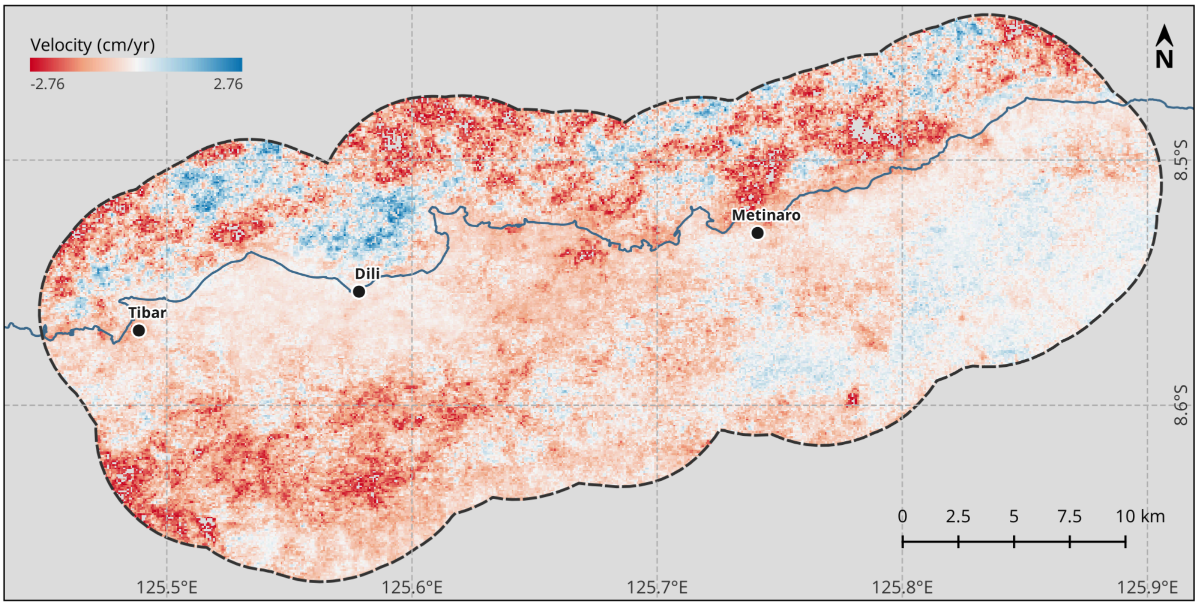

Figure 3. *InSAR-derived mean line-of-sight velocity across the study area, 2017 to 2026, from Sentinel-1 SBAS time-series inversion. Negative values (red) indicate subsidence; positive values (blue) indicate uplift. Values*

are displayed at a symmetric ±2.76 cm/yr range, corresponding to the 1st percentile of the data, to limit the visual influence of isolated extreme pixels; the full range is −4.91 to +3.55 cm/yr.

Zonal subsidence rate exhibited strong positive spatial autocorrelation (Global Moran's I = 0.7896, p = 0.001, 999 permutations). Local Indicators of Spatial Association identified 5,933 zones (46.4%) as members of a significant spatial cluster or outlier: 2,525 zones (19.8%) formed part of a low-low (subsidence) cluster, 3,305 zones (25.9%) formed part of a high-high (stable or uplifting) cluster, and 103 zones (0.8%) were spatial outliers (52 high-low, 51 low-high) (Figure 4).

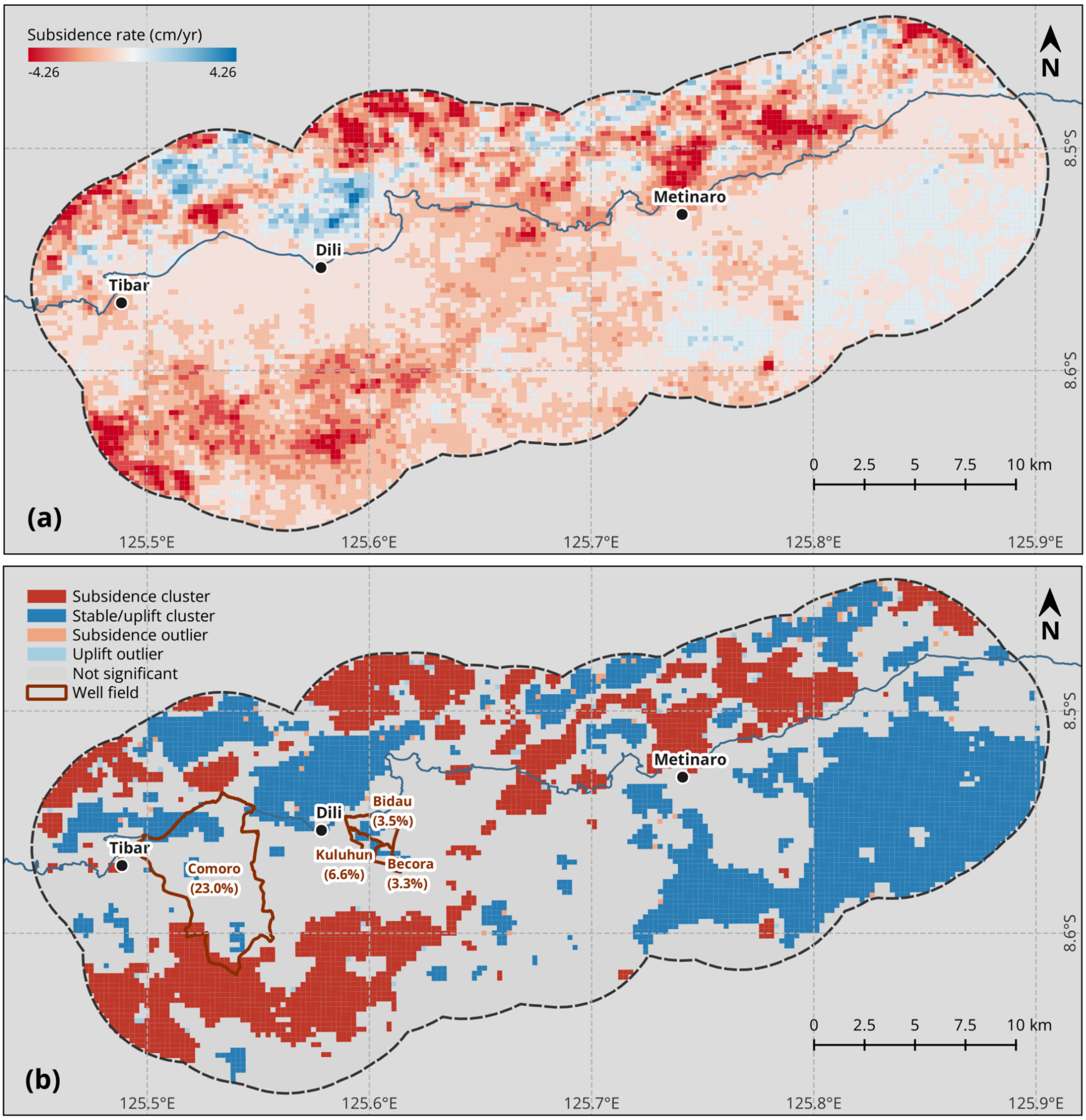

Figure 4. *Zonal subsidence across the 250 m analysis grid (n = 12,781 zones). (a) Mean subsidence rate per zone. (b) Local Indicators of Spatial Association (LISA) cluster classification, showing subsidence (low-low) clusters, stable or uplifting (high-high) clusters, and spatial outliers, at p < 0.05 from 999 permutations.*

An uncontrolled spatial overlay of the four resolvable well-field locations against the LISA classification found no area overlap with subsidence-cluster zones for three of the four fields (Becora, Bidau, Kuluhun); Comoro, the field with the largest extraction share (23.0% of total borehole supply), showed 4.7% overlap. Overlap with the stable/uplift cluster ranged from 14.6% (Comoro) to 41.4% (Kuluhun) across the four fields.

Lagrange Multiplier diagnostics on the ordinary least squares (OLS) residuals indicated a Spatial Error Model (SEM) specification was preferred over a Spatial Lag specification (Robust LM-error = 27.34, $p < 0.001$; Robust LM-lag = 8.03, $p = 0.005$). Under OLS, all five predictors were significant at $p < 0.001$, including well-field extraction intensity (coefficient = 0.266×10^{-3}, $p < 0.001$), consistent with H1's motivating groundwater-extraction mechanism. Under the properly specified SEM, however, well-field extraction intensity lost significance entirely and its coefficient shrank toward zero and reversed sign (coefficient = -0.098×10^{-3}, $p = 0.412$); distance to road showed the same pattern (SEM $p = 0.769$, versus OLS $p < 0.001$). A heteroskedasticity-robust SEM variant returned consistent results for both predictors (Table 2). Elevation, built-up density, and distance to coast remained significant across all three specifications. The spatial error autocorrelation parameter was high in both SEM variants (lambda = 0.9468, standard; lambda = 0.9498, z = 172.49, $p < 0.001$, heteroskedasticity-robust variant), indicating that most of subsidence's spatial structure is unexplained by the five predictors tested. H1's groundwater-extraction framing is therefore not supported once spatial autocorrelation is properly controlled for; elevation, built-up density, and distance to coast are the only predictors that remain robust attribution-regression correlates of subsidence rate in this dataset.

Table 2. *Attribution regression of zonal subsidence rate: OLS vs. Spatial Error Model (250 m grid, n = 12,781 zones).*

Predictor	OLS coef. ($\times 10^{-3}$)	OLS p	SEM coef. ($\times 10^{-3}$)	SEM p	SEM-Het coef. ($\times 10^{-3}$)	SEM-Het p
Elevation	0.692	<0.001***	0.908	0.003**	0.905	<0.001***
Built-up density	0.494	<0.001***	0.215	0.006**	0.215	<0.001***
Well-field extraction intensity	0.266	<0.001***	−0.098	0.412	−0.096	0.322
Distance to road	0.527	<0.001***	−0.102	0.769	−0.090	0.820
Distance to coast	−0.720	<0.001***	−1.024	0.023*	−1.022	0.006**
λ (spatial error parameter)	—	—	0.9468	—	0.9498	<0.001 (z=172.49)

*Note. All predictors standardized; coefficients rescaled $\times 10^{-3}$ for readability. *p<0.05, **p<0.01, ***p<0.001. Lagrange Multiplier diagnostics selected the Spatial Error Model over Spatial Lag: Robust LM-error = 27.34 (p<0.001) exceeded Robust LM-lag = 8.03 (p=0.005) (following the criterion of Anselin et al., 1996). SEM fitted via GM_Error (Kelejian–Prucha); SEM-Het = heteroskedasticity-robust variant (GM_Error_Het). Under proper spatial control, well-field extraction intensity and distance-to-road lose statistical significance and their coefficients shrink toward zero; elevation, built-up density, and distance-to-coast remain robust across all three specifications.*

4.2 RQ2: Mangrove Extent Change

Mangrove extent along Dili's coastline increased significantly over both time series tested, contrary to H2's predicted decline. Over the full 1996 to 2020 record (11 epochs), extent showed a significant increasing trend (Mann-Kendall $p = 0.013$; Theil-Sen slope = 1.08 ha/yr on a real calendar-year axis). Over a 2007 to 2020 robustness subset excluding the earliest epoch, the increasing trend remained significant ($p = 0.049$; Theil-Sen slope = 0.82 ha/yr), indicating the trend is not solely an artefact of the 1996 baseline. The 1996 epoch itself (449.1 ha, against a 474 to 488 ha range for all other epochs) is flagged as a likely product of sparser Landsat-era input relative to the denser multi-sensor compositing used from 2007 onward, rather than a confirmed ecological baseline (Figure 5).

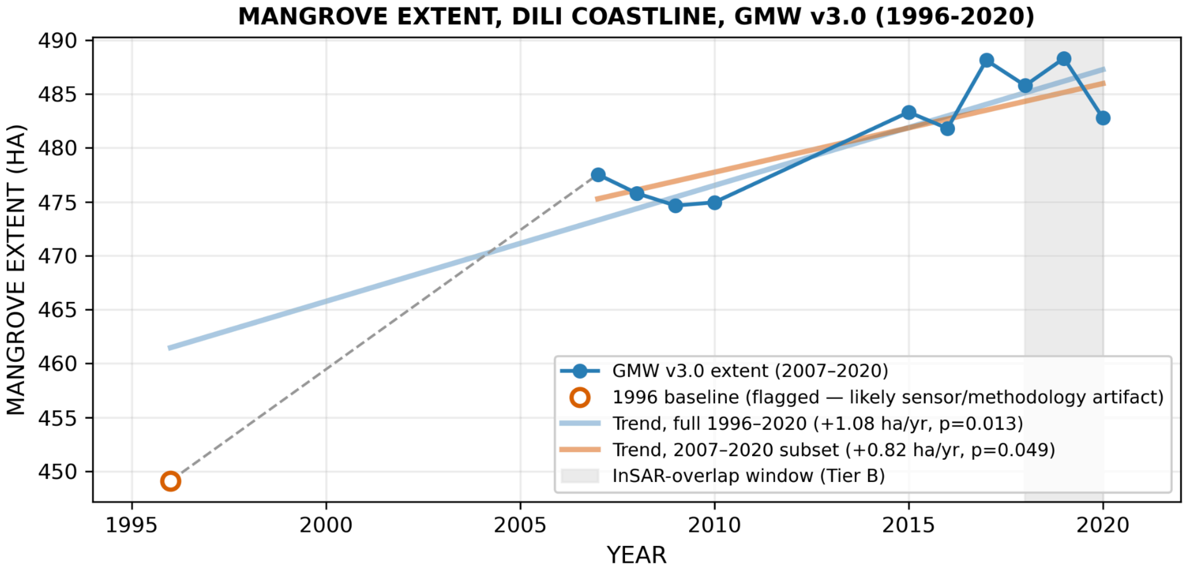

Figure 5. *Mangrove extent along Dili's coastline across the eleven Global Mangrove Watch v3.0 epochs, 1996 to 2020. The 1996 baseline is plotted separately and flagged as a likely sensor and methodology artefact rather than a confirmed ecological baseline. Theil-Sen trend lines are shown for the full 1996 to 2020 series and for the 2007 to 2020 robustness subset, with slopes and Mann-Kendall p-values. The shaded band marks the 2018 to 2020 window over which the mangrove and InSAR records overlap.*

Geometric loss/gain overlay across all epoch pairs found that gross turnover substantially exceeds net change at every transition; for example, the 2016 to 2017 transition shows a net gain of 6.3 ha comprising 12.0 ha gained against 5.7 ha lost. Dili's mangrove coastline is therefore under continuous, active reworking rather than simply stable or uniformly growing: net change alternates in direction from one transition to the next (5 of 9 non-baseline transitions show net loss, 4 show net gain). The most recent tracked transition, 2019 to 2020, shows the largest net decline in the series (−5.5 ha); over the direct 2018 to 2020 span used for the InSAR-overlap analyses, mangrove loss (12.58 ha) similarly outweighed gain (9.57 ha), a net decline of −3.0 ha (Figure 6). The 1996 to 2007 transition (+43.2 ha) is more than three times any other single-pair change, consistent with the 1996 epoch's flagged data quality distinction, and is not treated as comparable to the other nine transitions.

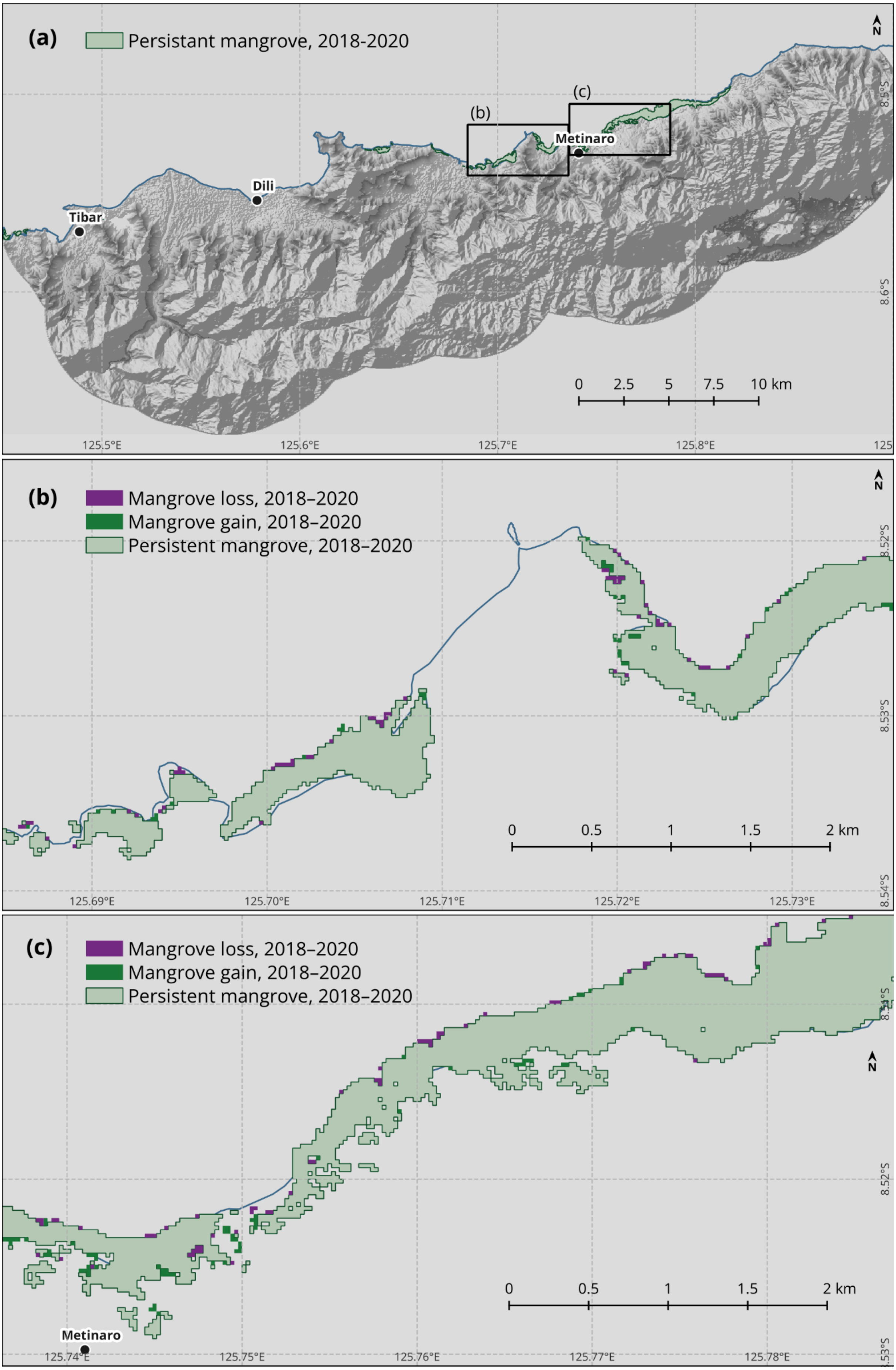

(a)
Persistant mangrove, 2018-2020
(b)
(c)
Metinaro
Dili
Tibar
0
2.5
5
7.5
10 km
125.5°E
125.6°E
125.7°E
125.8°E
8.5°S
8.6°S
(b)
Mangrove loss, 2018–2020
Mangrove gain, 2018–2020
Persistent mangrove, 2018–2020
0
0.5
1
1.5
2 km
125.69°E
125.70°E
125.71°E
125.72°E
125.73°E
8.52°S
8.53°S
8.54°S
(c)
Mangrove loss, 2018–2020
Mangrove gain, 2018–2020
Persistent mangrove, 2018–2020
0
0.5
1
1.5
2 km
Metinaro
125.74°E
125.75°E
125.76°E
125.77°E
125.78°E
8.52°S

Figure 6. *Mangrove transition in Dili, 2018 to 2020, derived from direct geometric overlay of the 2018 and 2020 Global Mangrove Watch v3.0 epochs. (a) Study area overview showing persistent mangrove cover and the locations of the two detail windows. (b, c) Detail windows over the eastern coastline, showing mangrove loss (12.58 ha), gain (9.57 ha), and persistent cover (473.21 ha) across the study area as a whole, for a net change of −3.0 ha. The two windows are representative sections selected for the density of change they contain and do not show all areas of turnover; further loss and gain occur elsewhere along the coast, including a separate cluster near Tibar. Both detail panels are drawn at a common scale. Stepped patch boundaries reflect the raster origin of the GMW v3.0 product at approximately 25 m resolution. Coordinates are shown in WGS 84; all areal calculations were performed in UTM Zone 51S (EPSG:32751).*

4.3 RQ3: Spatial Coincidence and Combined Risk Profile

Of the 210 zones containing 2018 mangrove extent (of 12,781 zones total), 86 (41.0%) fell within a subsidence-cluster zone, roughly twice the AOI-wide rate (19.8%); no mangrove-present zone fell within a stable/uplift-cluster zone, despite that classification covering 25.9% of the study area overall (Figure 7). This categorical spatial coincidence between mangrove presence and subsidence clustering is consistent with H3.

A continuous per-zone mangrove loss rate (2018 to 2020), however, showed a different pattern once small-denominator noise was accounted for. Spearman's rank correlation between mangrove loss rate and subsidence rate was significant for the full 210-zone sample (rho = -0.187, p = 0.007, in the hypothesis-consistent direction given subsidence is signed negative), but non-significant once zones with a 2018 baseline area under 0.5 ha were excluded (n = 157; rho = -0.076, p = 0.342). The substantial drop in both magnitude and significance indicates the full-sample correlation was driven by measurement noise in small-baseline zones rather than a robust continuous relationship. RQ3/H3 is therefore only partially supported: the categorical spatial coincidence is robust, while the continuous loss-rate relationship is not.

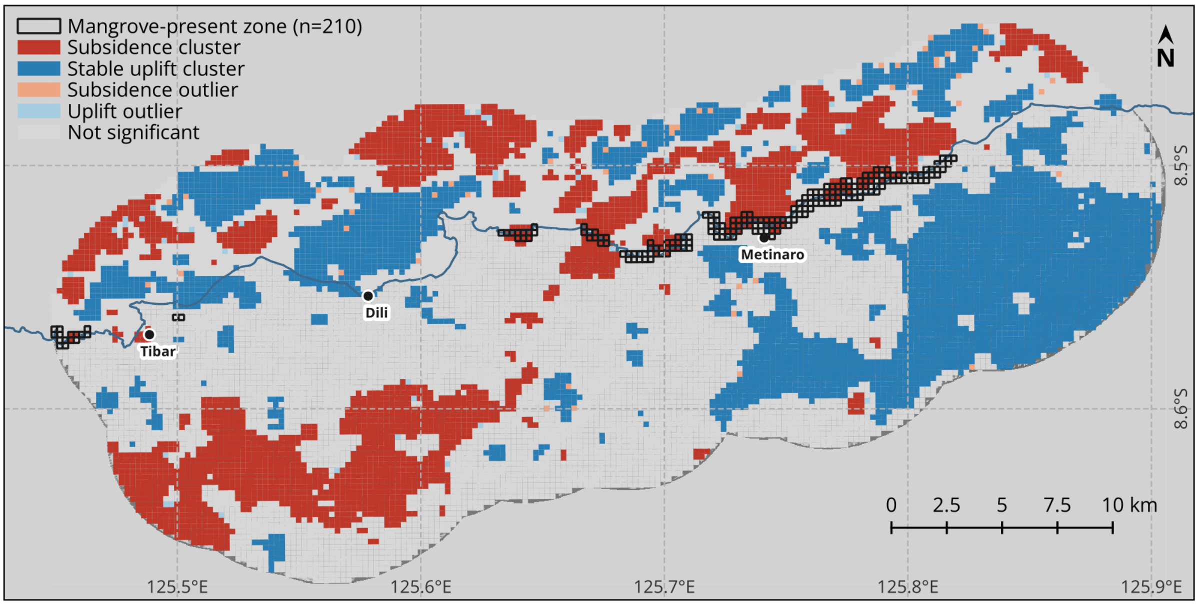

Figure 7. *Spatial coincidence between mangrove presence and subsidence clustering. Zones containing 2018 mangrove extent (n = 210) are shown as outlines against the LISA cluster classification of the full 250 m grid. Mangrove-present zones fall within subsidence clusters at 41.0%, approximately twice the study-area-wide rate of 19.8%, and none fall within the stable uplift cluster, which covers 25.9% of the study area. Coordinates are shown in WGS 84; all analysis was performed in UTM Zone 51S (EPSG:32751).*

4.4 RQ4: Exploratory Attribution

Using the RQ3-filtered zone set (baseline ≥ 0.5 ha, n = 157), high- and low-subsidence groups were compared under two independent split specifications. A median split (78 high-subsidence, 79 low-subsidence zones) found no significant difference in mangrove loss rate, either unadjusted (Mann-Whitney U, p = 0.208) or adjusted for land-use conversion pressure (OLS coefficient = 0.845, p = 0.472). A tertile split (52 high-subsidence, 53 low-subsidence zones, middle third excluded) likewise found no significant difference (Mann-Whitney U, p = 0.307; adjusted OLS coefficient = 0.753, p = 0.638), with the point estimate running slightly opposite to H4's predicted direction, though not meaningfully given the non-significance. No support for H4 was found across either specification, consistent with H4's exploratory framing (Figure 8).

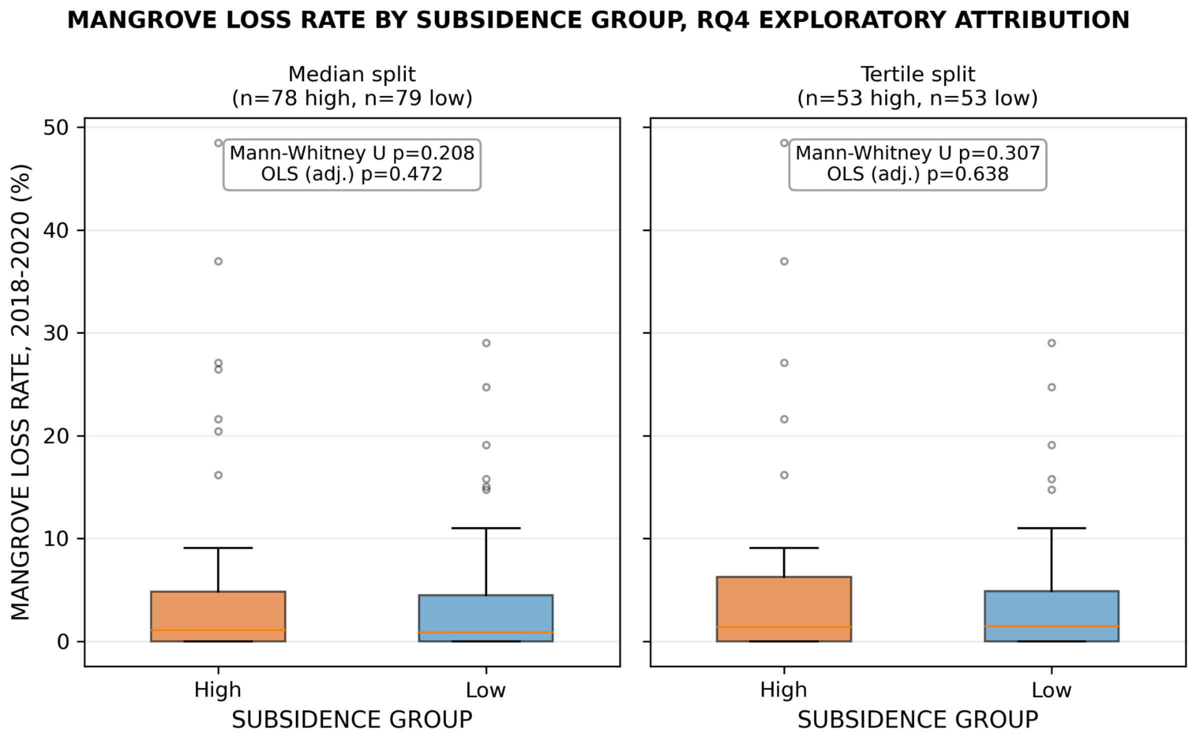

Figure 8. *Distribution of mangrove loss rate (2018 to 2020) between high- and low-subsidence zones under two independent split specifications: a median split (n = 78 high, 79 low) and a tertile split with the middle third excluded. Annotated p-values are from unadjusted Mann-Whitney U tests and from OLS regression adjusted for land-use conversion pressure. The tertile grouping shown was reconstructed from per-zone outputs and differs from the analysis grouping by one zone (53 versus 52 in the high-subsidence group), reflecting a boundary tie-handling difference; reported p-values are taken from the original analysis. No significant difference was found under either specification.*

4.5 Compound Future Relative Sea-Level Exposure

Combining each zone's Theil-Sen subsidence slope with NASA/IPCC AR6 sea-level-rise projections yields raw regional SLR estimates of 0.21 m (SSP2-4.5) and 0.24 m (SSP5-8.5) by 2050, rising to 0.59 m and 0.81 m respectively by 2100. Adding the observed subsidence contribution, median compound relative SLR across zones reaches 0.31 to 0.34 m by 2050 (13.9% to 17.2% of zones exceeding 0.5 m; 0.05% to 0.12% exceeding 1.0 m) and 0.91 to 1.13 m by 2100 (88.9% to 96.0% of zones exceeding 0.5 m; 41.5% to 63.7% exceeding 1.0 m; 13.4% to 22.2% exceeding 1.5 m; 3.7% to 6.7% exceeding 2.0 m) (Figure 9). The time-horizon effect (2050 versus 2100) dominates the scenario effect (SSP2-4.5 versus SSP5-8.5) at either horizon. These figures extrapolate the observed geodetic subsidence rate up to 74 years beyond the approximately nine-year observation window, from an SLR source point approximately 85 to 90 km from Dili, and should be read as a bounded trend extrapolation rather than a predictive scenario model (Section 3.7).

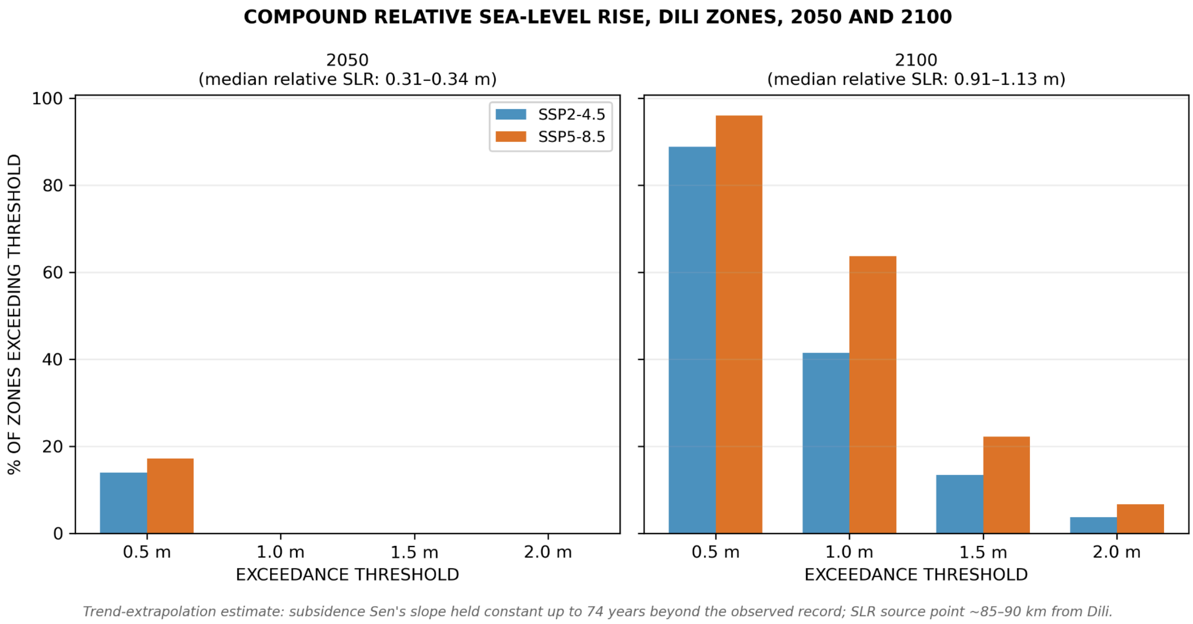

Figure 9. *Compound future relative sea-level exposure, combining per-zone observed subsidence rate with NASA/IPCC AR6 regional sea-level projections, under two emissions scenarios (SSP2-4.5 and SSP5-8.5) at two horizons (2050 and 2100). Bars show the proportion of zones exceeding 0.5, 1.0, 1.5, and 2.0 m of compound relative sea-level rise.*

5. Discussion

5.1 Land Subsidence: Magnitude, Pattern, and the Groundwater-Extraction Question

Dili's mean subsidence rate of -0.53 cm/yr, with a maximum of -4.26 cm/yr, is modest relative to the well-documented sinking cities of Southeast Asia. Recent InSAR-based estimates place Jakarta's subsidence at 1 to 11 cm/yr and Semarang's at 2 to 3 cm/yr, with some sub-districts of the wider Semarang-Demak area reaching over 10 cm/yr (Susilo et al., 2023). Ho Chi Minh City shows a comparable order of magnitude: an early ALOS-based PSI study measured an average of 0.8 cm/yr and a maximum of 7 cm/yr for 2006 to 2010 (Minh et al., 2015), while a more recent Sentinel-1-based study covering 2017 to 2019 found a lower average of 0.33 cm/yr and a maximum of 5.3 cm/yr (Duffy et al., 2020), a decline the authors attribute in part to measures taken to reduce groundwater extraction in the intervening years. Dili's rate is real and spatially structured, but an order of magnitude gentler than the maxima reported for any of these three cities, consistent with a much smaller and less intensively pumped urban aquifer.

The attribution regression result is harder to characterise simply. An uncontrolled comparison of subsidence rate against well-field proximity initially suggested extraction was associated with less, not more, subsidence, the opposite of H1's motivating mechanism. Once spatial autocorrelation was properly modelled, however, this relationship disappeared entirely rather than reversing into a confirmed protective effect: well-field extraction intensity's coefficient shrank toward zero and lost significance under the Spatial Error Model. This outcome should not be read as evidence that groundwater extraction does not drive subsidence in Dili. Rather, it reflects a resolution mismatch between a zonal, well-field-level extraction proxy and a subsurface process that can vary sharply over short distances. In the Mekong Delta, spatial variation in groundwater-driven subsidence has been attributed to subsurface heterogeneity in aquifer architecture and sediment properties that a delta-wide model, let alone a single zonal predictor, could not fully resolve (Minderhoud et al., 2017). The very high spatial error parameter recovered here (lambda approximately 0.95) points in the same direction: most of the spatial structure in Dili's subsidence signal is not explained by any of the five predictors tested, consistent with an unmeasured, finer-grained hydrogeological process rather than a straightforward absence of a groundwater-extraction effect. A further contributing factor is likely under-representation in the extraction proxy itself: in many developing Southeast Asian capitals, municipal borehole records capture only a fraction of total groundwater abstraction, with unmonitored private, commercial, and household wells widespread. If this holds for Dili, the well-field predictor would understate the true spatial footprint of extraction, independent of any hydrogeological heterogeneity.

5.2 Local Mangrove Increase Against the National Narrative

The significant increasing trend in mangrove extent along Dili's coastline, both across the full 1996-2020 record and the 2007-2020 robustness subset, runs directly counter to H2 and to the national-level narrative of substantial mangrove decline that partly motivated this study. Read in isolation, this result might appear anomalous. Read against recent global evidence, it is not. A comprehensive four-decade satellite assessment recently found that global mangrove cover shifted from net loss to net gain around 2010, driven in large part by natural recolonisation of abandoned aquaculture ponds and expansion into newly accreting coastal mudflats, with Indonesia specifically identified as having halted its steep historical decline after 2005 (Zhang et al., 2026). Dili's own increasing trend begins within this same window and continues through 2020, timing broadly consistent with a regional turning point rather than a Dili-specific artefact.

This reframing does not resolve the tension with Section 1's motivating national narrative so much as relocate it: an aggregate national decline measured primarily against pre-1940 baselines is compatible with a recovering or stabilising coastal segment observed more recently, particularly if direct land-use pressures such as aquaculture conversion have eased locally. The transition analysis adds an important qualification to this optimistic reading. Gross turnover substantially exceeds net change at every epoch transition, meaning Dili's coastline is not passively stable but under continuous, active reworking; net direction alternates transition to transition, and the long-term increasing trend is a cumulative-magnitude effect rather than one of consistent expansion, with the most recent transition showing the sharpest net decline recorded. Whether this dynamic favours long-term net gain depends on drivers this study cannot directly observe, and should not be assumed to continue indefinitely.

5.3 Coincidence Versus Correlation: What RQ3 Does and Does Not Show

RQ3 produced two findings that point in different directions on the strength of the subsidence-mangrove spatial relationship. Categorically, mangrove-present zones fall within subsidence-cluster zones at roughly twice the AOI-wide rate, and no mangrove-present zone falls within a stable or uplifting cluster at all, a striking pattern consistent with H3. Continuously, however, the degree of subsidence does not reliably track the degree of mangrove loss once small-denominator noise is removed. Taken together, these results are best explained by shared geomorphology rather than a demonstrated causal relationship. Mangroves are ecologically confined to a narrow intertidal envelope, typically between mean sea level and the highest spring tide (Ma et al., 2020), which is by definition low-lying coastal terrain. Elevation was independently confirmed as a robust, significant predictor of subsidence rate in the attribution regression (Section 4.1). The same low-elevation zones that host Dili's remaining mangroves are therefore also the zones most likely to register measurable subsidence, without either process needing to cause the other.

This distinction matters for how the combined risk picture motivated in Section 1 should be read. The categorical coincidence is real and policy-relevant: a materially large share of Dili's remaining mangrove extent sits within zones independently confirmed to be subsiding. But the mechanism connecting the two is best understood, on current evidence, as a shared physical setting rather than subsidence actively degrading mangrove condition, a distinction directly relevant to interpreting RQ4.

5.4 The Absent Subsidence-Mangrove Stress Signal

RQ4 found no support for a subsidence-driven contribution to mangrove loss, across two independent group-split specifications and both unadjusted and covariate-adjusted tests. Given H4's explicitly exploratory framing, this null result is informative rather than merely inconclusive, but it should not be read as ruling out the mechanism it tested. Sea-level-rise-driven mangrove stress operates through a sediment-accretion deficit: mangroves can keep pace with relative sea-level rise only if vertical soil accretion matches or exceeds it, and even at sites where this deficit is severe, complete submergence has been projected to take until as early as 2070, not months or a few years (Lovelock et al., 2015). RQ4's analysis window, the 2018-2020 InSAR-overlap period, spans only two years, considerably shorter than the timescale over which an accretion deficit would be expected to manifest as detectable canopy loss. Dili's subsidence magnitude is also modest relative to regional comparators (Section 5.1), which may place it below whatever threshold, if one exists, is needed for a measurable stress signal to emerge over such a short window. The absence of a detectable effect at this magnitude and duration is therefore best read as inconclusive with respect to the underlying mechanism, not as evidence against it.

5.5 Compound Future Exposure and the Twin-Indicator Synthesis

This study set out to examine subsidence and mangrove loss as parallel, independently-driven signals of coastal vulnerability, testing rather than assuming any link between them. On that basis, the twin-indicator framing has held up, though not in the way either motivating hypothesis anticipated. H1's groundwater-extraction mechanism did not survive proper spatial control, though the underlying subsidence signal itself is real and well-resolved. H2's predicted decline was directly contradicted by an increasing trend consistent with a broader, only recently documented regional recovery. Yet the two indicators converge spatially in a way that matters for coastal management regardless of either individual hypothesis's outcome: Dili's remaining mangroves and its subsidence hotspots occupy the same low-lying coastal terrain, and the compound sea-level-rise projections in Section 4.5 show that, by 2100, this terrain could face relative sea-level rise exceeding 0.5 m across the large majority of zones under either emissions scenario. Whether or not subsidence is ever shown to directly stress the mangroves growing atop it, the two processes are unfolding in the same physical space, which is precisely the combined risk picture the twin-indicator design was intended to surface.

6. Conclusion

This study provided the first satellite-based, twin-indicator assessment of coastal vulnerability in Dili, Timor-Leste, pairing Sentinel-1 InSAR time series analysis of land subsidence with Global Mangrove Watch mangrove-extent change over a multi-decadal baseline. Subsidence was detected across the urban coastal footprint, spatially heterogeneous and strongly autocorrelated, but its attribution to groundwater extraction specifically did not survive proper spatial statistical control, leaving H1's motivating mechanism unresolved rather than confirmed or refuted. Mangrove extent increased significantly over both the full 1996-2020 record and a 2007-2020 robustness subset, directly counter to H2's predicted decline, a result consistent with a broader, recently documented regional and global shift from mangrove loss toward mangrove recovery. Subsidence and mangrove presence showed a robust categorical spatial coincidence but no robust continuous relationship, and no evidence emerged for a direct subsidence-driven contribution to mangrove loss over the short InSAR-overlap window available for testing.

These findings represent the first satellite geodetic measurement of land subsidence anywhere in Timor-Leste and the first multi-epoch, satellite-based mangrove change-detection study conducted for Dili's coastline within an explicit coastal-vulnerability framing. The cloud-based InSAR processing pipeline used here, built on free, on-demand services rather than local high-performance computing, offers a low-cost, hardware-independent template that other researchers working in similarly data- and resource-scarce small-island settings could reasonably adapt.

Several limitations bound how these results should be read. The analysis is confined to Dili's coastal footprint and does not characterise subsidence or mangrove change at the national scale. All data are satellite-derived, with no field validation of either the InSAR displacement estimates or the mangrove classification. The

InSAR-mangrove overlap window used for the comparative and exploratory analyses spans only two years, which limits the statistical power available to detect a subsidence-mangrove relationship even where one might exist. The compound sea-level-rise estimates extrapolate a nine-year observed subsidence trend up to 74 years forward and should be read as a bounded projection rather than a scenario-based forecast. None of these limitations undermine the core findings reported, but each narrows the scope of what those findings can be generalised to claim.

Future work could usefully target the specific gaps this study leaves open: finer-resolution or in-situ groundwater monitoring to test the attribution question that zonal InSAR alone could not resolve, extension of the InSAR record to lengthen the mangrove-overlap window as further Sentinel-1 and future GMW epochs become available, and field-based validation of both the subsidence and mangrove-extent products. More broadly, this study demonstrates that even where a study's original motivating hypotheses are not confirmed, in this case a groundwater-extraction mechanism that did not hold up and a decline that did not materialise, a twin-indicator satellite framework can still surface a genuine, policy-relevant finding: that Dili's remaining mangroves and its zones of active subsidence occupy the same low-lying coastal terrain, a convergence that will matter for coastal planning as relative sea levels continue to rise.

Acknowledgements

The author gratefully acknowledges the providers of the freely available datasets used in this study: the Sentinel-1 Single Look Complex archive, provided by the European Space Agency; the Global Mangrove Watch version 3.0 dataset, made available by Bunting et al. (2022) via the Global Mangrove Watch platform; the Copernicus Digital Elevation Model (GLO-30), provided by the European Space Agency; the Global Human Settlement Layer GHS-BUILT-S product, provided by the European Commission's Joint Research Centre; ERA5 reanalysis data, provided by the European Centre for Medium-Range Weather Forecasts via the Copernicus Climate Change Service; well-field borehole-share data, reported by Sarmento and Da Cruz Cardoso (2014); the IPCC AR6 Sea Level Projections dataset, made available by Garner et al. (2021) via Zenodo; the Database of Global Administrative Areas (GADM v4.1); and OpenStreetMap road and coastline geometry, provided by OpenStreetMap contributors. Processing of the Sentinel-1 interferometric time series was performed using the Alaska Satellite Facility's HyP3 on-demand processing service and OpenSARLab cloud computing environment, both provided by the Alaska Satellite Facility, University of Alaska Fairbanks. The analysis was conducted independently, and the findings, interpretations, and conclusions expressed in this paper are those of the author alone.

Data Availability

This study's derived geospatial datasets, tabular outputs, and analysis code are openly available on Zenodo at [https://doi.org/10.5281/zenodo.21807825] under a Creative Commons Attribution 4.0 International licence. Raw input datasets are publicly available from their respective providers: the Sentinel-1 Single Look Complex archive, accessed via the Copernicus Data Space Ecosystem (https://dataspace.copernicus.eu/); the Global Mangrove Watch version 3.0 dataset, made available by Bunting et al. (2022) via Zenodo (https://zenodo.org/records/6894273); the Copernicus Digital Elevation Model, GLO-30 (https://doi.org/10.5270/ESA-c5d3d65); the Global Human Settlement Layer GHS-BUILT-S product, provided by the European Commission's Joint Research Centre (https://ghsl.jrc.ec.europa.eu/); ERA5 reanalysis data, accessed via the Copernicus Climate Data Store (https://cds.climate.copernicus.eu/); the IPCC AR6 Sea Level Projections dataset, made available by Garner et al. (2021) via Zenodo (https://doi.org/10.5281/zenodo.5914709); the Database of Global Administrative Areas, version 4.1 (https://gadm.org/); and OpenStreetMap road and coastline geometry (https://www.openstreetmap.org/). Well-field borehole-share data were sourced from the published values reported in Sarmento and Da Cruz Cardoso (2014) rather than from a standalone downloadable dataset. Empirical analysis, InSAR time series processing, and visualisation were conducted in Python and its libraries, the Alaska Satellite Facility's HyP3 and OpenSARLab processing services, MintPy, and QGIS, as described in Section 3.

Declaration of Competing Interest

The author declares that there are no conflicts of interest with respect to the research, authorship, or publication of this article. No financial or personal relationships with any organisation or individual have influenced the work reported herein. This research received no external funding.

Ethics Statement

This research did not involve human participants, animal subjects or any form of clinical intervention. All datasets used are publicly available secondary remote-sensing and geospatial products. Ethical approval was not required and is not applicable for this study.

References

Alongi, D. M. (2014). Mangrove forests of Timor-Leste: Ecology, degradation and vulnerability to climate change. In I. Faridah-Hanum, A. Latiff, K. R. Hakeem, & M. Ozturk (Eds.), Mangrove ecosystems of Asia: Status, challenges and management strategies (pp. 199–211). Springer. https://doi.org/10.1007/978-1-4614-8582-7_9

Anselin, L. (1995). Local indicators of spatial association—LISA. Geographical Analysis, 27(2), 93–115. https://doi.org/10.1111/j.1538-4632.1995.tb00338.x

Anselin, L., Bera, A. K., Florax, R., & Yoon, M. J. (1996). Simple diagnostic tests for spatial dependence. Regional Science and Urban Economics, 26(1), 77–104. https://doi.org/10.1016/0166-0462(95)02111-6

Berardino, P., Fornaro, G., Lanari, R., & Sansosti, E. (2002). A new algorithm for surface deformation monitoring based on small baseline differential SAR interferograms. IEEE Transactions on Geoscience and Remote Sensing, 40(11), 2375–2383. https://doi.org/10.1109/TGRS.2002.803792

Bunting, P., Rosenqvist, A., Hilarides, L., Lucas, R. M., Thomas, N., Tadono, T., Worthington, T. A., Spalding, M., Murray, N. J., & Rebelo, L.-M. (2022). Global mangrove extent change 1996–2020: Global Mangrove Watch version 3.0. Remote Sensing, 14(15), Article 3657. https://doi.org/10.3390/rs14153657

Carruthers, L., Ersek, V., Maher, D., Sanders, C., Tait, D., Soares, J., Floyd, M., Hashim, A. S., Helber, S., Garnett, M., East, H., Johnson, J. A., Ponta, G., & Sippo, J. Z. (2024). Sea-level rise and extreme Indian Ocean Dipole explain mangrove dieback in the Maldives. Scientific Reports, 14, Article 27012. https://doi.org/10.1038/s41598-024-73776-z

da Costa Belo, J., Calheiros, T., & Gonzalez Pereira, M. (2026). Climate change in Timor-Leste: A systematic review and meta-analysis through a multi-scale regional lens. Climate, 14(7), Article 148. https://doi.org/10.3390/cli14070148

Duffy, C. E., Braun, A., & Hochschild, V. (2020). Surface subsidence in urbanized coastal areas: PSI methods based on Sentinel-1 for Ho Chi Minh City. Remote Sensing, 12(24), Article 4130. https://doi.org/10.3390/rs12244130

European Space Agency. (2022). Copernicus Digital Elevation Model [Data set]. https://doi.org/10.5270/ESA-c5d3d65

Fattahi, H., & Amelung, F. (2013). DEM error correction in InSAR time series. IEEE Transactions on Geoscience and Remote Sensing, 51(7), 4249–4259. https://doi.org/10.1109/TGRS.2012.2227761

GADM. (2026). Database of Global Administrative Areas, version 4.1. https://gadm.org

Garner, G. G., Hermans, T., Kopp, R. E., Slangen, A. B. A., Edwards, T. L., Levermann, A., Nowicki, S., Palmer, M. D., Smith, C., Fox-Kemper, B., Hewitt, H. T., Xiao, C., Aðalgeirsdóttir, G., Drijfhout, S. S., Golledge, N. R., Hemer, M., Krinner, G., Mix, A., Notz, D., … Pearson, B. (2021). IPCC AR6 sea level projections (Version 20210809) [Data set]. Zenodo. https://doi.org/10.5281/zenodo.5914709

Hamed, K. H., & Rao, A. R. (1998). A modified Mann-Kendall trend test for autocorrelated data. Journal of Hydrology, 204(1–4), 182–196. https://doi.org/10.1016/S0022-1694(97)00125-X

Harris, R. (2011). The nature of the Banda arc-continent collision in the Timor region. In D. Brown & P. D. Ryan (Eds.), Arc-continent collision (Frontiers in Earth Sciences, pp. 163–211). Springer. https://doi.org/10.1007/978-3-540-88558-0_7

Herrera-García, G., Ezquerro, P., Tomás, R., Béjar-Pizarro, M., López-Vinielles, J., Rossi, M., Mateos, R. M., Carreón-Freyre, D., Lambert, J., Teatini, P., Cabral-Cano, E., Erkens, G., Galloway, D., Hung, W.-C., Kakar, N., Sneed, M., Tosi, L., Wang, H., & Ye, S. (2021). Mapping the global threat of land subsidence. Science, 371(6524), 34–36. https://doi.org/10.1126/science.abb8549

Hersbach, H., Bell, B., Berrisford, P., Hirahara, S., Horányi, A., Muñoz-Sabater, J., Nicolas, J., Peubey, C., Radu, R., Schepers, D., Simmons, A., Soci, C., Abdalla, S., Abellan, X., Balsamo, G., Bechtold, P., Biavati, G., Bidlot, J., Bonavita, M., … Thépaut, J.-N. (2020). The ERA5 global reanalysis. Quarterly Journal of the Royal Meteorological Society, 146(730), 1999–2049. https://doi.org/10.1002/qj.3803

Kelejian, H. H., & Prucha, I. R. (1999). A generalized moments estimator for the autoregressive parameter in a spatial model. International Economic Review, 40(2), 509–533. https://doi.org/10.1111/1468-2354.00027

Kelejian, H. H., & Prucha, I. R. (2010). Specification and estimation of spatial autoregressive models with autoregressive and heteroskedastic disturbances. Journal of Econometrics, 157(1), 53–67. https://doi.org/10.1016/j.jeconom.2009.10.025

Lovelock, C. E., Cahoon, D. R., Friess, D. A., Guntenspergen, G. R., Krauss, K. W., Reef, R., Rogers, K., Saunders, M. L., Sidik, F., Swales, A., Saintilan, N., Thuyen, L. X., & Triet, T. (2015). The vulnerability of Indo-Pacific mangrove forests to sea-level rise. Nature, 526(7574), 559–563. https://doi.org/10.1038/nature15538

Ma, W., Wang, W., Tang, C., Chen, G., & Wang, M. (2020). Zonation of mangrove flora and fauna in a subtropical estuarine wetland based on surface elevation. Ecology and Evolution, 10(14), 7404–7418. https://doi.org/10.1002/ece3.6467

Mann, H. B. (1945). Nonparametric tests against trend. Econometrica, 13(3), 245–259. https://doi.org/10.2307/1907187

Menéndez, P., Losada, I. J., Torres-Ortega, S., Narayan, S., & Beck, M. W. (2020). The global flood protection benefits of mangroves. Scientific Reports, 10, Article 4404. https://doi.org/10.1038/s41598-020-61136-6

Minderhoud, P. S. J., Erkens, G., Pham, V. H., Bui, V. T., Erban, L., Kooi, H., & Stouthamer, E. (2017). Impacts of 25 years of groundwater extraction on subsidence in the Mekong delta, Vietnam. Environmental Research Letters, 12(6), Article 064006. https://doi.org/10.1088/1748-9326/aa7146

Minderhoud, P. S. J., Shirzaei, M., & Teatini, P. (2025). From InSAR-derived subsidence to relative sea-level rise—A call for rigor. Earth's Future, 13, Article e2024EF005539. https://doi.org/10.1029/2024EF005539

Minh, D. H. T., Van Trung, L., & Toan, T. L. (2015). Mapping ground subsidence phenomena in Ho Chi Minh City through the radar interferometry technique using ALOS PALSAR data. Remote Sensing, 7(7), 8543–8562. https://doi.org/10.3390/rs70708543

Molyneux, N., Rangel da Cruz, G., Williams, R. L., Andersen, R., & Turner, N. C. (2012). Climate change and population growth in Timor Leste: Implications for food security. Ambio, 41(8), 823–840. https://doi.org/10.1007/s13280-012-0287-0

Moran, P. A. P. (1950). Notes on continuous stochastic phenomena. Biometrika, 37(1–2), 17–23. https://doi.org/10.1093/biomet/37.1-2.17

OpenStreetMap contributors. (2026). Planet dump. OpenStreetMap Foundation. https://www.openstreetmap.org

Pesaresi, M., Schiavina, M., Politis, P., Freire, S., Krasnodębska, K., Uhl, J. H., Carioli, A., Corbane, C., Dijkstra, L., Florio, P., Friedrich, H. K., Gao, J., Leyk, S., Lu, L., Maffenini, L., Mari-Rivero, I., Melchiorri, M., Syrris, V., Van Den Hoek, J., & Kemper, T. (2024). Advances on the Global Human Settlement Layer by joint assessment of Earth Observation and population survey data. International Journal of Digital Earth, 17(1). https://doi.org/10.1080/17538947.2024.2390454

Richards, D. R., & Friess, D. A. (2016). Rates and drivers of mangrove deforestation in Southeast Asia, 2000–2012. Proceedings of the National Academy of Sciences, 113(2), 344–349. https://doi.org/10.1073/pnas.1510272113

Sarmento, D. R., & Da Cruz Cardoso, J. B. (2014). Risk assessment for groundwater resources in Dili, the capital city of Timor-Leste. International Journal of Interdisciplinary and Multidisciplinary Studies, 1(10), 180–191.

Sen, P. K. (1968). Estimates of the regression coefficient based on Kendall's tau. Journal of the American Statistical Association, 63(324), 1379–1389. https://doi.org/10.1080/01621459.1968.10480934

Susilo, S., Salman, R., Hermawan, W., Widyaningrum, R., Wibowo, S. T., Lumban-Gaol, Y. A., Meilano, I., & Yun, S.-H. (2023). GNSS land subsidence observations along the northern coastline of Java, Indonesia. Scientific Data, 10, Article 421. https://doi.org/10.1038/s41597-023-02274-0

(2023). Subsidence reveals potential impacts of future sea level rise on inhabited mangrove coasts. Nature Sustainability. https://doi.org/10.1038/s41893-023-01226-1

van Bijsterveldt, C. E. J., Herman, P. M. J., van Wesenbeeck, B. K., Ramadhani, S., Heuts, T. S., van Starrenburg, C., Tas, S. A. J., Triyanti, A., Helmi, M., Tonneijck, F. H., & Bouma, T. J. Subsidence reveals potential impacts of future sea level rise on inhabited mangrove coasts. *Nat Sustain* 6, 1565–1577 (2023). https://doi.org/10.1038/s41893-023-01226-1

Wu, P.-C., Wei, M., & D'Hondt, S. (2022). Subsidence in coastal cities throughout the world observed by InSAR. Geophysical Research Letters, 49(7), Article e2022GL098477. https://doi.org/10.1029/2022GL098477

Yunjun, Z., Fattahi, H., & Amelung, F. (2019). Small baseline InSAR time series analysis: Unwrapping error correction and noise reduction. Computers & Geosciences, 133, Article 104331. https://doi.org/10.1016/j.cageo.2019.104331

Zhang, Z., Murray, N. J., Song, X.-P., Bunting, P., Worthington, T. A., Fatoyinbo, L., Mao, D., Jia, M., Arifanti, V. B., Aung, T., Htay, S. S., & Friess, D. A. (2026). Unexpected expansion and regrowth in Earth's mangrove forests over the past four decades. Science, 392(6802), 1082–1087. https://doi.org/10.1126/science.aec9773